OPEN

Interfacial growth of large-area single-layer metal-organic framework nanosheets

Rie Makiura[1,2,3] & Oleg Konovalov[4]

[1]Nanoscience and Nanotechnology Research Center, Research Organization for the 21st Century, Osaka Prefecture University, Sakai, Osaka 599-8570, Japan, [2]PRESTO, Japan Science and Technology Agency, Saitama, Japan, [3]CREST, Japan Science and Technology Agency, Saitama, Japan, [4]European Synchrotron Radiation Facility, Grenoble, Cedex 38043, France.

The air/liquid interface is an excellent platform to assemble two-dimensional (2D) sheets of materials by enhancing spontaneous organizational features of the building components and encouraging large length scale in-plane growth. We have grown 2D molecularly-thin crystalline metal-organic-framework (MOF) nanosheets composed of porphyrin building units and metal-ion joints (NAFS-13) under operationally simple ambient conditions at the air/liquid interface. *In-situ* synchrotron X-ray diffraction studies of the formation process performed directly at the interface were employed to optimize the NAFS-13 growth protocol leading to the development of a post-injection method –post-injection of the metal connectors into the water subphase on whose surface the molecular building blocks are pre-oriented– which allowed us to achieve the formation of large-surface area morphologically-uniform preferentially-oriented single-layer nanosheets. The growth of such large-size high-quality sheets is of interest for the understanding of the fundamental physical/chemical properties associated with ultra-thin sheet-shaped materials and the realization of their use in applications.

N anomaterials, which can be obtained as atomically thin two-dimensional (2D) sheets have been attracting considerable attention[1–7], especially after the isolation of graphene[8,9], for addressing fundamental issues related to their strictly 2D electronic structure and for enabling their integration in nanotechnological devices, such as transparent electrodes for optical devices and active sheets for sensors. Besides graphene, the preparation of 2D inorganic nanosheets of titanium and niobium oxides, and lead sulfide has been also reported[10–12] together with that of 2D polymer nanosheets composed of only organic components prepared by solvent-induced delamination of organic crystals[13]. Nonetheless, the rational fabrication of atomically or molecularly thin 2D nanonetworks with large lateral size and uniform morphology is a major challenge and is still at an early stage of development. The importance of the availability of such large-surface area uniform nanosheets is that they can be ultimate components for nanodevices with as small as necessary amount of material. In addition, unique properties, such as lowering of phase transition temperatures[14] and realization of 2D electron gas[15] encountered at the nanoscale or at interfaces are attractive for obtaining new functionalities. Finally, the nanosheets can be layered resulting in the facile creation of 3D multi-layered structures with tailored thickness and permitting the development of heterostructures at the nanoscale. The common methodology in isolating such nanosheets is the physical/chemical exfoliation of layer-structured bulk materials. The number of layers which defines the thickness can be tuned by the exfoliation conditions[16–18]. Exfoliation is a promising method for obtaining 2D nanosheets because the starting bulk laminar crystals can be prepared by conventional large scale synthesis[17–19]. However, the ultimate goal in this field is the preparation of 2D nanosheets by direct bottom-up approach in order to achieve fine control of their size (number of building units in the in-plane direction) and shape at the nanoscale without the need of any further treatment such as delamination, suspension, or alignment on a substrate[1,20].

Highly-ordered porous organic-inorganic hybrid compounds, so called metal–organic frameworks (MOFs) or porous coordination polymers (PCPs) have been receiving considerable attention. The rich variety of materials arising from the unlimited possible combinations of metal ions and organic ligands and the presence of regulated pores and cavities can lead to a number of potential applications ranging from industrial use to medical purposes[21–25]. For instance, selective gas adsorption and separation[26], highly reactive catalytic activities[27], and efficient molecular storage/transfer/release functionalities for drug delivery[28] have been reported. However, MOFs are

typically obtained as insoluble and unprocessable powders by conventional synthetic techniques such as solvothermal/hydrothermal methods. Therefore, aligning them on various surfaces in desired ways and controlling their size and dimensionality at the nanoscale have remained as important challenges.

In fact, reports on various attempts to process bulk polycrystalline MOFs and to fabricate nanoscaled ones by developing new methodologies such as microwave synthesis, inverse emulsion technique, and liquid phase epitaxy, have been increasing in recent years[29–41]. Especially, 2D sheet assemblies are necessary when considering the use of such coordination materials, which frequently incorporate functional π-electron components, in nanotechnological thin film devices. We have ourselves recently succeeded in preparing a family of crystalline perfectly-oriented MOF thin films with nanometer scale thickness derived from metalloporphyrin building units and metal ion connectors (NAFS: nanofilms of metal–organic frameworks on surfaces) using a bottom-up solution-based method, which combines the Langmuir–Blodgett and the layer-by-layer (LB-LbL) methodologies at ambient conditions[36–38]. The NAFS family of materials have layered structures, comprising 2D molecular networks, which are first assembled at the air/liquid interface in a Langmuir trough (Langmuir-Blodgett (LB) films)[42], then transferred to a solid surface by horizontal dipping, and finally stacked sequentially following a layer-by-layer (LbL) film deposition protocol[36–38].

Applying the LB technique to hard molecular components without any soft alkyl chains had been reported before using π-electron molecular units with flat shape, which float on the liquid surface of the Langmuir trough and form LB film assemblies[43–47]. However, since such π-electron flat molecules easily self-stack, the obtained films are invariably characterized by densely packed structural motifs – their formation driven by the stabilization of the intermolecular interactions – of individual molecules standing at an angle to the air/liquid interface. Employing functionalized molecules as the spreading substance and aqueous solutions of metal salts as a subphase to supply the connecting units was expected to allow the formation of metal-mediated molecular arrays[45–47]. However, no direct structural evidence at the molecular level for such an alignment pattern had been ever reported before. Our strategy for obtaining MOF sheets was to devise chemical reactions at the 2D interface by aligning the molecular entities two dimensionally in such a way that each component adopted ideal topological proximity and separation distances that could lead to the creation of cavities and the development of porosity. The coordinative architecture of the NAFS family of nanofilms was directly proven by synchrotron X-ray crystallography – the films were endowed with highly crystalline order not only in the out-of-plane but also in the in-plane orientation with the flat molecular building units aligned with their planar parts parallel to the surface.

Thus employing air/liquid interfaces on which to assemble MOF nanosheets is a highly promising technique as the 2D interface encourages in-plane growth over a large length scale and the liquid substrate enhances spontaneous organizational features of the building components[10,48,49]. In order to develop the strategy of growing 2D molecularly-thin morphologically-uniform nanoassemblies of hard molecules with fine control of domain size and molecular arrangement, in-depth understanding of the *in-situ* sheet formation mechanism associated with the coordinative bonding linkages between the building blocks and the connecting joints is essential. Preliminary insight into the formation process of MOF nanofilms prepared at the air/liquid interface and transferred onto solid substrates in a sequential layer-by-layer manner has been obtained by *ex-situ* characterization techniques[50].

Herein we make use of *in-situ* synchrotron X-ray crystallographic techniques together with input by complementary Brewster angle microscopy and X-ray reflectivity measurements to probe directly the lateral assembly of single-molecule thin nanonetworks of a new member of the NAFS family (NAFS-13, *vide infra*) at the air/liquid interface. We demonstrate that crystalline NAFS-13 nanosheets perfectly oriented with their planar parts parallel to the air/liquid interface form under operationally simple ambient conditions on the liquid surface of a Langmuir trough. We then establish a growth protocol – post-injection of the metal connector units into the water subphase on the surface of which the molecular building units are pre-oriented – which achieves excellent crystallinity, uniform film morphology, and significant enlargement of the average crystalline sheet domain size. Creation of such highly-regulated uniform nanosheets, large enough to connect patterned electrodes or to obtain as free standing films, offers the possibility of their use in applications such as ultra-thin electronic devices[51,52] and molecular/ion filters[53,54].

Results

Nanosheet growth. Our procedure for preparing molecule-thin crystalline MOF sheets starts with the spreading of a solution of molecular building units (metalloporphyrin, 5,10,15,20-tetrakis(4-carboxyphenyl)-porphyrinato-palladium(II) (PdTCPP, **1**) in chloroform/methanol) onto a subphase of metal ion joints (aqueous solution of $Cu(NO)_3 \cdot 3H_2O$, **2**) at the air/water interface of a Langmuir trough (Fig. 1 and Supporting Information). The formation of the two-dimensional (2D) copper-mediated PdTCPP arrays (NAFS-13) is followed by measuring the surface pressure - mean molecular area (π-A) isotherm as the surface is compressed to a pressure of 40 mN/m by moving the barrier walls of the trough at a constant speed (Fig. 1, red line). The observed π-A isotherm of the NAFS-13 PdTCPP-Cu sheet is in good accord with those of the CoTCPP-py-Cu (NAFS-1)[36] and H2TCPP-Cu (NAFS-2)[38] analogues providing evidence that the linkage motif responsible for sheet formation is also the same – namely, linking of the tetratopic PdTCPP molecules occurs *via* copper ion joints and the resulting arrays lie flat on the air/water interface. When for comparison the same PdTCPP solution was spread onto a pure water subphase in the Langmuir trough and compressed at the same barrier speed, the mean molecular area, *A* measured at the same surface pressure, π was significantly smaller (Fig. 1, black line). This implies that either the PdTCPP molecules now stand vertically at some angle to the liquid surface or remain in the horizontal orientation but pack more closely. It also confirms the necessity of the Cu^{2+} ion joints for film formation. The PdTCPP sheet arrangements consistent with the π-A isotherm measurements are supported by UV-visible absorption spectroscopy measurements on films formed at a surface pressure of 10 mN/m and deposited onto quartz substrates by horizontal dipping (Fig. S1a). The absorbance of the characteristic Soret band of the porphyrin units measured for the PdTCPP sheet formed on pure water is higher than that for the array fabricated on copper ion aqueous solution, implying a larger surface packing density of PdTCPP molecules.

In-situ **grazing incidence X-ray diffraction.** Detailed insight into the formation and in-plane order, parallel to the liquid surface, of the NAFS-13 sheets prepared in a dedicated Langmuir trough mounted on the six-circle diffractometer at the ESRF beamline, ID10B was obtained from *in-situ* synchrotron XRD (λ = 1.549 Å) measurements. These were carried out directly at the air/liquid interface in grazing incidence (GI) in-plane mode with the incident beam nearly parallel to the liquid surface[55–57], as illustrated in Fig. 1. Fig. 2a shows the evolution of the in-plane GIXRD patterns measured for the NAFS-13 sheets with increasing surface pressure (π = 0, 1, 5, 10, 20, and 30 mN/m – the surface pressure, measured by the Wilhelmy plate method, was kept constant during each measurement). The observation of a number of sharp clearly-resolved Bragg peaks in the in-plane XRD profiles provides the signature of the formation of a large-scale structure with highly crystalline organization. Very importantly, the same profile is obtained at π ≈ 0 mN/m after initial
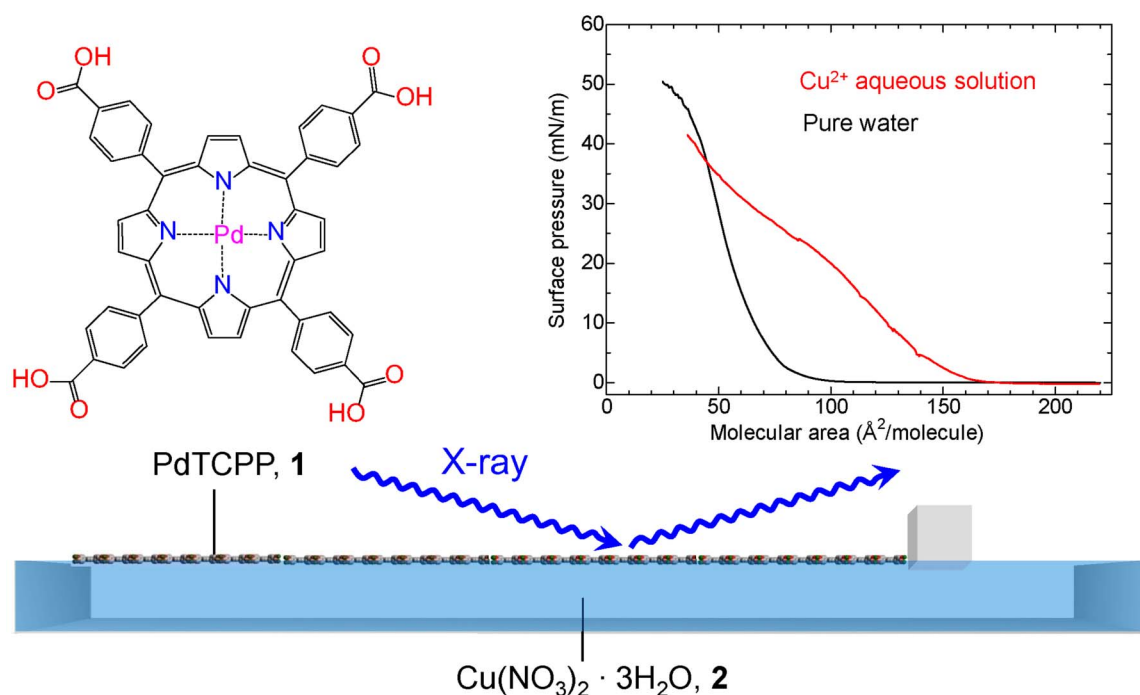
Figure 1 | Schematic illustration of the assembly process of PdTCPP-Cu metal-organic framework nanosheets (NAFS-13) at the air/liquid interface monitored by *in-situ* grazing incidence XRD (GIXRD) measurements. The solution of PdTCPP molecular building units, **1** is spread onto the Cu(NO$_3$)$_2$·3H$_2$O aqueous solution, **2** in a Langmuir trough. The surface pressure, π is controlled by the movement of a single one-side barrier and is kept constant during the collection of each GIXRD profile at the air/liquid interface. The inset shows surface pressure – mean molecular area (π-A) isotherms for NAFS-13 (red line) and for PdTCPP solution, 1 spread onto pure water subphase (black line).

spreading of the metalloporphyrin solution onto the copper ion subphase. This implies that formation of NAFS-13 sheets with excellent crystallinity and a high coherence length does not necessitate surface compression – it occurs in a self-assembling manner induced by the two-dimensional interfacial reaction between the copper ions and the carboxylic acid groups at the periphery of the PdTCPP molecular units. For comparison, we also performed *in-situ* GIXRD measurements at the air/liquid interface for PdTCPP arrays formed on a pure water subphase. The absence of Bragg reflections reveals the lack of molecular organization and absence of crystalline order in the PdTCCP arrays formed without the presence of copper ions in the subphase (Fig. S2). However, in this case as the surface pressure, π approaches higher values (π = 30 mN/m), there is gradual appearance of a broad diffuse scattering hump which peaks near Q_{xy} = 1.8–1.9 Å^{-1}. This corresponds to an intermolecular distance of about 3.3–3.5 Å, which is comparable to the typical π–π stacking distances between adjacent (metallo)porphyrin units and supports the physical picture developed from the UV spectra that the PdTCPP molecules are packed closely and stand vertically at some angle to the air/liquid interface.

All six observed peaks in the GIXRD profile (Fig. 2a) of the NAFS-13 nanosheet up to a scattering angle, 2θ = 30° (Q_{xy} = 2.1 Å^{-1}) index as (*hk*0) and correspond to (110), (200), (220), (320), (400), and (330) Bragg peaks of a metrically tetragonal unit cell with in-plane lattice parameters, $a = b ≈ 16.6$ Å. These are extremely close to those of the multilayered NAFS-1 and NAFS-2 thin films deposited on silicon substrates ($a = b = 16.5$ Å)[36,38]. The comparable lattice sizes signify that the in-plane molecular arrangement in NAFS-13 is also that of metalloporphyrin linkers and paddle-wheel dimeric Cu$_2$(COO)$_4$ secondary building units, which form a two-dimensional checkerboard pattern (Fig. 2b,c). The number of diffraction peaks remains the same as the surface is progressively compressed implying that the molecular organization of the NAFS-13 sheet is preserved intact upon increasing surface pressure. On the other hand, the position, width

and intensity of the Bragg reflections gradually evolve with surface compression (Fig. 2d–g). In the low surface pressure region, π = 0–1 mN/m and before π begins to increase sharply with decreasing mean molecular area, A, the unit cell size of the crystalline structure (a = 16.628(6) Å at 0 mN/m and 16.625(3) Å at 1 mN/m, Fig. 2e) and the average crystalline domain size (~140 nm, as estimated from the peak width of the most intense (110) peak using Scherrer's equation, Fig. 2f) of the NAFS-13 nanosheet do not change, indicating that there is little influence on the sheet assembly process by the surface compression. This contrasts with the behavior of the peak intensity, which increases sharply with compression in the same surface pressure range (Fig. 2g). This can be understood by considering that, upon spreading, the surface area is relatively large in comparison with the number of spread molecules. Therefore the effect of increasing surface compression is initially to increase the surface coverage by gathering the pre-assembled floating NAFS-13 domains to a smaller area without affecting the crystalline domain size. The growth in the intensity of the Soret band of the porphyrin units with increasing surface pressure (Fig. S1b) measured by UV-vis spectroscopy for NAFS-13 films formed at different compression and deposited onto quartz substrates supports this phenomenological interpretation.

However, further increase of the surface pressure has a more pronounced effect on both the crystalline structure of the nanosheets and their morphology. Firstly, the in-plane lattice parameter, a, contracts monotonically from 16.628(6) to 16.496(5) Å as π increases to 30 mN/m (Fig. 2e). This is accompanied by a decrease in the sheet domain size from 140(3) to 93(1) nm (Fig. 2f) and by the continuous growth of the intensity of the (110) Bragg reflection in the same surface pressure range (Fig. 2g). In order to understand this, we recall that as the surface compression increases, the coverage of the Langmuir trough surface increases until it is fully covered by the molecular sheets. Upon further compression, the sheets gather into a continuously decreasing area until their edge parts begin to touch neighboring sheets thereby leading to increased surface roughness
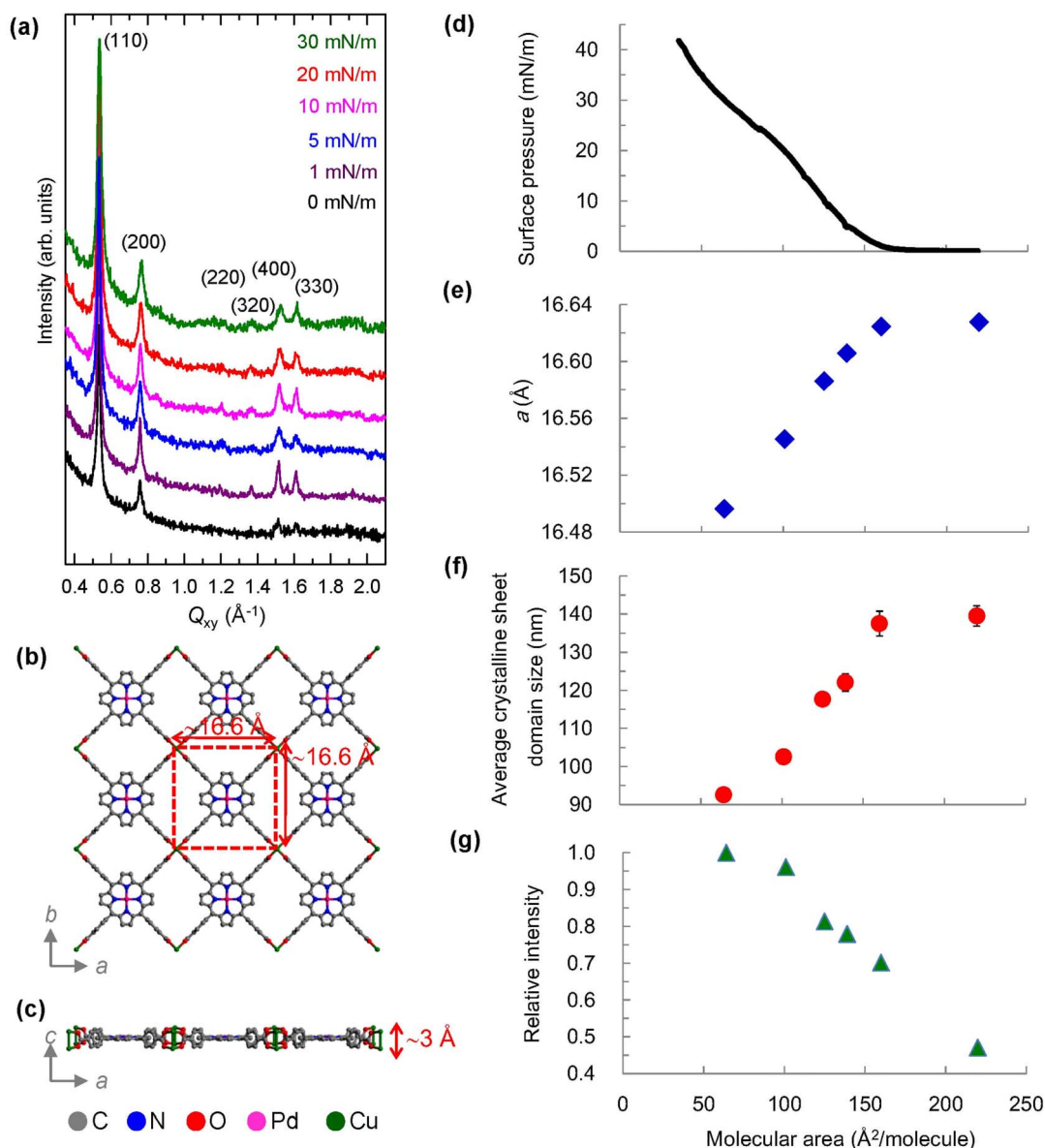
Figure 2 | *In-situ* grazing incidence in-plane synchrotron X-ray diffraction (GIXRD) patterns collected at the air/liquid interface for NAFS-13 nanosheets. (a), Observed GIXRD (λ = 1.549 Å, incidence angle, α = 0.12°) profiles at surface pressures, π = 0, 1, 5, 10, 20, and 30 mN/m. All six observed peaks up to a scattering angle, 2θ = 30° (Q_{xy} = 2.1 Å^{-1}) index as (hk0) on a metrically tetragonal unit cell with basal plane dimensions, $a = b \approx$ 16.6 Å (the Miller indices of the Bragg peaks are (110), (200), (220), (320), (400), and (330) in order of increasing scattering angle). (b), Basal plane projection of the crystalline structure of NAFS-13, which consists of a 2D "checkerboard" motif of PdTCPP units linked by binuclear $Cu_2(COO)_4$ paddle wheels. The red dashed lines mark the in-plane square unit cell. C atoms are shown in grey, N atoms in blue, O atoms in red, Pd^{2+} ions in pale pink, and Cu^{2+} ions in green color. (c), Schematic diagram of the crystalline structure of NAFS-13, which consists of 2D sheets of thickness $\sim$3 Å viewed along the b axis. (d–g), Evolution of the crystalline structure and morphology of the molecularly thin NAFS-13 nanofilms with change in surface compression. (d), Surface pressure – mean molecular area (π-A) isotherm. (e), Unit cell basal plane dimension, a, (f), average crystalline sheet domain size estimated from the full width at half maximum of the intense (110) Bragg reflection, and (g), relative intensity of the (110) reflection normalized to the value at the highest surface compression *versus* mean molecular area, A at surface pressures, π = 0, 1, 5, 10, 20, and 30 mN/m.

through deformations or multiple sheet stacking. This process can account for the accompanying evolution in lattice constant, average sheet domain size, and intensity of the Bragg peaks.

Complementary X-ray reflectivity (XRR) and Brewster angle microscopy (BAM) measurements of the NAFS-13 nanosheets and of the PdTCPP arrays formed on pure water subphase at various surface pressures also support this interpretation. Increased surface roughness generally causes a lowering of the XRR. Here the observed continuous decrease of XRR with increasing surface compression (Fig. S3 and S4) can be thus attributed to sheet morphology changes which lead to increased roughness. Similar conclusions can be drawn

by the recorded BAM images (Fig. S5). These show first progressively increasing coverage of the surface of the Langmuir trough by well-formed nanosheets upon compression, followed by development of cracks and surface morphology deformations at high surface pressures. Furthermore, white spots are observed in the BAM images even at the low compression stages implying the presence of some molecular aggregation in the sheets.

Discussion

Thus far the study of the formation of the PdTCPP-Cu MOF nanosheets at the air/liquid interface has revealed that the most

important step in the film assembly process is the interfacial coordinative reaction which occurs immediately after spreading the solution of the metalloporphyrin building units, **1** on the surface of the solution containing the metal ion joints, **2** – this is also the critical process in determining the sheet domain size. However, in the conventional assembly protocol of the NAFS-13 sheets that we applied here, it is unavoidable that, upon spreading, droplets of solution, **1** produce surface ripples and the spread molecules have the freedom
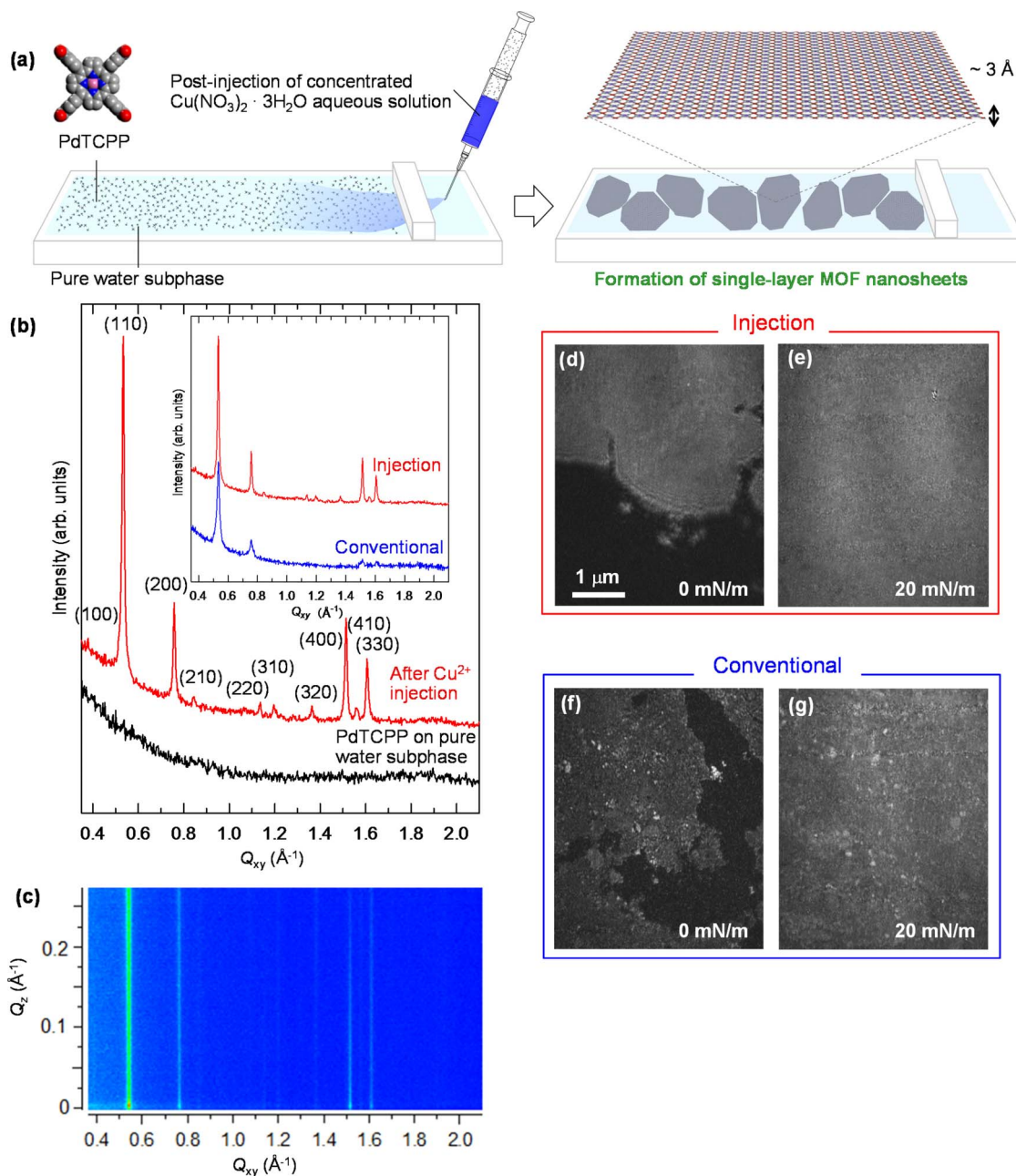
Figure 3 | Formation of large-area monomolecularly-thin NAFS-13 nanosheets assembled at the air/liquid interface by the post-injection method of the metal ion component. (a), Schematic illustration of the post-injection methodology employed in the fabrication of NAFS-13 nanosheets. A PdTCPP solution, **1** is first spread directly on the pure water subphase. A concentrated $Cu(NO_3)_2 \cdot 3H_2O$ aqueous solution (2.3 M), **2** is then slowly injected into the water subphase from the side surface, which is separated from the Langmuir trough by the compression barrier. (b), Observed grazing incidence in-plane synchrotron GIXRD profiles ($\lambda = 1.549$ Å, incidence angle, $\alpha = 0.12°$) for PdTCPP, **1** spread on the pure water subphase before (black line) and after (red line) injection of the $Cu(NO_3)_2 \cdot 3H_2O$ aqueous solution, **2** in the absence of barrier compression. All ten observed peaks after injection of the metal component up to a scattering angle, $2\theta = 30°$ ($Q_{xy} = 2.1$ Å^{-1}) index as ($hk0$) on a metrically tetragonal unit cell with basal plane dimensions, $a = b \approx 16.6$ Å (the Miller indices of the Bragg peaks are (100), (110), (200), (210), (220), (310), (320), (400), (410), and (330) in order of increasing scattering angle). The *inset* shows a comparison of the in-plane GIXRD profiles for the NAFS-13 nanosheets formed by the conventional method of Fig. 1a (blue line) and the post-injection method (red line) at $\pi = 0$ mN/m. (c), Grazing incidence X-ray diffraction reciprocal space map of the NAFS-13 nanosheets formed by the metal linkers post-injection method. Integration of the XRD map as a function of the vertical scattering vector, Q_z for the intense (110) Bragg reflection (Fig. S7) allows an estimate of the sheet thickness to be made as ~3 Å. (d–g), Brewster angle microscopy (BAM) images obtained with a green laser ($\lambda = 532$ nm) at an incident angle of 53.12° (Brewster angle) with respect to the air/water interface normal taken during the formation of the NAFS-13 nanofilms fabricated by the post-injection (d), (e) and the conventional (f), (g) methods at compressions, $\pi = 0$ and 20 mN/m. Additional BAM images collected during the post-injection NAFS-13 film formation are shown in Fig. S11.

to move rapidly around the surface. This is clearly captured by the BAM images, which show the random movement of the floating NAFS-13 domains before compression (Fig. S5). Such a procedure does not utilize past experience in successfully growing large single crystals of coordination compounds in the bulk where slow diffusion of the reactant solutions is invariably employed. Therefore, we have attempted to integrate slow diffusion protocols into the nanosheet growth strategy and developed a modification of the above methodology in order to target more optimal conditions for enlarging the sheet domain size and avoiding any aggregation. As illustrated in Fig. 3a, we first spread the solution of the molecular building units, **1** directly on the pure water subphase, and then gently inject the copper ion metal joint solution, **2** into the subphase.

After spreading the PdTCPP solution but before the copper ion injection, the in-plane XRD profile collected on the water surface is featureless with no Bragg peaks present (Fig. 3b, black line). This confirms that PdTCPP molecules do not self-assemble to form a crystalline sheet without copper ion linkers. Formation of hydrogen bonded networks on solid substrate surfaces such as Au(111) and HOPG has been reported for the analogous porphyrin with four peripheral carboxylic groups, 5,10,15,20-tetrakis(4-carboxylphenyl)-21H,23H-porphyrin (H$_2$TCPP)[58,59]. We consider that the lack of formation of a comparable array of self-assembled PdTCPP molecules is related to the presence at the air/water interface of a considerable number of water molecules, which surround the PdTCPP units and prevent formation of H-bonded COOH networks.

After injecting the concentrated copper ion solution into the subphase, a number of very sharp well-resolved peaks emerge in the GIXRD profile (Fig. 3b, red line), implying the formation of NAFS-13 nanosheets with excellent lateral crystalline structural order in the absence of barrier compression. The observed Bragg peaks and their positions coincide with those recorded for the NAFS-13 nanosheet formed by the conventional method on pre-contained Cu^{2+} solution subphase at $\pi = 0$ mN/m (inset Fig. 3b). This confirms the adoption of the same crystalline sheet structure with identical lattice constants (16.620(2) vs 16.628(6) Å, respectively; Fig. S8). Very importantly, however, the peak widths of the Bragg reflections in the GIXRD pattern of the nanosheet assembled by the injection method are now considerably smaller (for the most intense (110) reflection, FWHM = 0.011 Å^{-1}) than those observed for the nanosheet prepared earlier by the conventional method (FWHM = 0.017 Å^{-1}) (Fig. S7), thereby reflecting a significant increase in the lateral size of the crystalline domains. The sheet domain size estimated using Scherrer's formula is now about 220 nm in length corresponding to a more than doubling of the average area of individual NAFS-13 domains by adopting the post-injection film growth method – each domain now contains on the order of twenty thousand molecular building units. At the same time, the resolution of a number of additional Bragg peaks (inset Fig. 3b) confirms the formation of nanofilms with superior crystalline structural order using the new methodology (Fig. S8).

Additional information about the molecular organization of the NAFS-13 nanofilms is obtained by 2D grazing incidence X-ray diffraction patterns, $i.e.$ reciprocal space maps of the diffracted intensity along orthogonal Q_{xy} (horizontal) and Q_z (vertical) diffraction vector axes. As shown in Fig. 3c, the scattered intensity for each reflection is seen as a scattering rod, which is strictly parallel to the Q_z axis. This provides unambiguous evidence that the NAFS-13 nanosheets are perfectly oriented with the 2D sheet plane aligned parallel to the liquid surface. At the same time, integrated out-of-plane line scans for each Bragg reflection as a function of scattering vector, Q_z provide information on the out-of-plane coherence length and therefore allow an estimate of the sheet thickness to be made. Figure S7 shows the broad Q_z profile of the (110) reflection integrated in the range, $Q_{xy} = 0.51$–0.55 Å^{-1}. The coherence length and therefore the sheet thickness can be then estimated as 3.2(2) Å from the fitted FWHM of

the out-of-plane profile. This is in good agreement with the thickness of a single metalloporphyrin building unit (Fig. 2c), thereby confirming that NAFS-13 is essentially a mono-molecularly thin nanosheet.

The trends in the evolution of the lattice parameter, the average sheet domain size, and the intensity of the Bragg peaks with increasing surface pressure mimic those observed for the NAFS-13 nanosheets prepared by the conventional method (Fig. S8). Nonetheless, the sheet domain size for NAFS-13 assembled by the post-injection method remains significantly larger at all surface pressures (Fig. S8b). The observed changes in the XRR curves recorded before and after injection (Fig. S10) confirm that reaction of the PdTCPP molecules with the injected copper ions results in the formation of NAFS-13 sheets with different film thickness and morphology from those of the PdTCPP arrays on the pure water subphase. In addition, the recorded BAM images of NAFS-13 formed by the post-injection method (Fig. S11) reveal (i) a much smoother sheet morphology (Fig. 3d, e) than that of the conventionally assembled sheets (Fig. 3f, g) and (ii) a complete absence of white spots associated with the existence of molecular aggregations which were evident even at the beginning of the sheet formation stage ($\pi \approx 0$ mN/m) for the conventionally formed NAFS-13. Therefore surface rippling and immediate reaction at the interface not only limit sheet domain growth but also lead to the creation of bulk aggregates restricting the formation of smooth 2D sheets. On the other hand, the slow injection growth method we developed leads to enlarged sheet domain sizes at the microscopic level, while at the same time provides smooth surface morphology of the mono-molecularly thin sheets at the macroscopic level.

In the work presented here, we have studied the formation of the porphyrin-based MOF nanosheets, NAFS-13, by in-$situ$ GIXRD at the air/liquid interface. The results reveal that the highly-crystalline preferentially-oriented ultranarrow NAFS-13 sheets form immediately after spreading the molecular building units on the copper ion aqueous solution subphase. Surface compression results in gathering these crystalline domains together, and leads to an increase in surface coverage but also to a decrease in the average domain size. Following the insight obtained on the nanosheet formation process, a new approach of sheet assembly – post-injection of the metal linkers into the subphase – was developed that effectively led to the enlargement of the NAFS-13 sheet domain size. The new methodology also resulted in the generation of smooth surface of the sheets at the micrometer scale. Sheet domain size and surface roughness strongly influence the properties of molecularly-thin 2D materials (molecular separation, electronic/ionic/photo conduction, magnetism) – these have to be carefully tuned when one considers them for use in nano-devices. The bottom-up sheet growth technique at the air/liquid interface we demonstrated here is sufficiently versatile to open the way for the facile transfer of the prepared large-size uniform ultra-thin 2D structures on various planar substrates while retaining their excellent crystallinity. We will investigate the transfer of the nanosheets on suitable solid substrates and layer them with other types of 2D nanosheets such as graphene, metal oxides, and organic polymers with the aim of achieving the creation of multifunctional 2D systems in future work.

Methods

Materials. 5,10,15,20-tetrakis(4-carboxyphenyl)-porphyrinato palladium(II) (PdTCPP, **1**) was purchased from Frontier Scientific or Sigma-Aldrich Co. Cu(NO$_3$)$_2$·3H$_2$O (>99.9%, **2**) was purchased from Waco Pure Chemical Industries Ltd or Sigma-Aldrich Co. Pure grades of chloroform and methanol were purchased from Waco Pure Chemical Industries Ltd or Sigma-Aldrich Co. All chemicals were used as received without further treatment.

Sheet preparation. A PTFE-coated Langmuir trough (460 × 170 × 5 mm³) was filled with an aqueous solution of Cu(NO$_3$)$_2$·3H$_2$O, **2** (1 mM) as a subphase. The surface of the subphase was carefully cleaned by mild surface-touch vacuuming. 260 μL of 0.2 mM solution of PdTCPP, **1** in mixed chloroform/methanol solvent (3 : 1, v/v) was spread onto the Cu(NO$_3$)$_2$ subphase with a microsyringe. Surface pressure–area (π-

6

A) isotherm measurements were performed at a continuous pressing speed for the barrier of 500 µm/s at room temperature. The surface pressure was measured with the Wilhelmy plate method. 300 µL of the same 0.2 mM PdTCPP solution was also spread onto a pure water subphase and π-A isotherms were measured for comparison. For the post-injection film growth method, the 0.2 mM PdTCPP, **1** solution was first directly spread onto a pure water subphase. Then 200 µL of a concentrated aqueous solution of Cu(NO$_3$)$_3$·3H$_2$O, **2** (2.3 M) was slowly injected with a microsyringe from the side surface into the water subphase while keeping the compression barrier fully open. The final concentration of the Cu(NO$_3$)$_3$·3H$_2$O, **2** aqueous solution after injection was 1 mM. The barrier was again moved at the same pressing speed of 500 µm/s at room temperature.

Brewster angle microscopy (BAM). Formation and morphology of the sheets in the Langmuir trough were followed by BAM experiments performed with a NIMA Technology BAM model 712 system in which a PTFE Langmuir trough (750 × 100 mm^2) with two compression barriers was installed. The PdTCPP-based films were prepared as described above. The laser wavelength was 532 nm. The incidence angle of the laser light was adjusted to 53.12° (magnitude of the Brewster angle for the air/water interface) with respect to the surface normal. Images of the films at the air/liquid interface were captured by a CCD camera at room temperature.

Grazing-incidence synchrotron X-ray diffraction (GIXRD) and X-ray reflectivity (XRR) measurements. In-situ synchrotron GIXRD and XRR measurements were performed at room temperature with the six-circle diffractometer on beamline ID10B (E = 8.003 keV, λ = 1.549 Å) at the ESRF (Grenoble, France). The dedicated PTFE Langmuir trough (460 × 170 × 5 mm^3) mounted on the diffractometer was equipped with a single movable barrier for film compression. The PdTCCP-based films were prepared as described above. The surface pressure was kept constant during individual GIXRD and XRR measurements. The Langmuir trough was mounted on an active antivibration system and was enclosed inside an air-tight acrylic case with polyimide windows. Water-saturated helium gas was introduced into the case. The incidence angle for the GIXRD measurements was set as 0.12°. The scattered X-rays were recorded by an one-dimensional (1D) gas-filled position-sensitive detector with vertically located counting wires (VANTEC). The XRD profiles were collected by scanning over the in-plane θ angle and the vertical (out-of-plane) scattered intensity was recorded at each 2θ angle. In order to improve the 2θ resolution to the in-plane direction and reduce background contribution, a Soller collimator (0.08°) was placed in front of the 1D detector. XRR data were collected by a two-dimensional (2D) gas-filled position-sensitive detector at the glancing angular range by a θ–2θ scan in the out-of-plane geometry. The average sheet domain size was estimated with Scherrer's equation using a value for Scherrer's constant of 1.84, appropriate for (*hk*) Bragg reflections of layer-structured crystalline materials.

1. Barth, J. V., Costantini, G. & Kern, K. Engineering atomic and molecular nanostructures at surfaces. *Nature* **437**, 671–679 (2005).
2. Elemans, J. A. A. W., Lei, S. & De Feyter, S. Molecular and Supramolecular Networks on Surfaces: From Two-Dimensional Crystal Engineering to Reactivity. *Angew. Chem. Int. Ed.* **48**, 7298–7332 (2009).
3. Sakamoto, J., Van Heijst, J., Lukin, O. & Schlüter, A. D. Two-Dimensional Polymers: Just a Dream of Synthetic Chemists? *Angew. Chem. Int. Ed.* **48**, 1030–1069 (2009).
4. Joensen, P., Frindt, R. F. & Morrison, S. R. Single-layer MoS$_2$. *Mater. Res. Bull.* **21**, 457–461 (1986).
5. Schlickum, U. *et al.* Metal-Organic Honeycomb Nanomeshes with Tunable Cavity Size. *Nano Lett.* **7**, 3813–3817 (2007).
6. Madueno, R., Räisänen, M. T., Silien, C. & Buck, M. Functionalizing hydrogen-bonded surface networks with self-assembled monolayers. *Nature* **454**, 618–621 (2008).
7. Wang, Q. H. & Hersam, M. C. Room-temperature molecular-resolution characterization of self-assembled organic monolayers on epitaxial graphene. *Nature Chem.* **1**, 206–211 (2009).
8. Novoselov, K. S. *et al.* Two-dimensional gas of massless Dirac fermions in graphene. *Nature* **438**, 197–200 (2005).
9. Geim, A. K. & Novoselov, K. S. The rise of graphene. *Nature Mater.* **6**, 183–191 (2007).
10. Akatsuka, K. *et al.* Construction of Highly Ordered Lamellar Nanostructures through Langmuir–Blodgett Deposition of Molecularly Thin Titania Nanosheets Tens of Micrometers Wide and Their Excellent Dielectric Properties. *ACS Nano* **3**, 1097–1106 (2009).
11. Osada, M. *et al.* Robust High-κ Response in Molecularly Thin Perovskite Nanosheets. *ACS Nano* **4**, 5225–5232 (2010).
12. Acharya, S. *et al.* A Bottom-Up Approach toward Fabrication of Ultrathin PbS Sheets. *Nano Lett.* **13**, 409–415 (2013).
13. Kissel, P. *et al.* A two-dimensional polymer prepared by organic synthesis. *Nature Chem.* **4**, 287–291 (2012).
14. Makiura, R. *et al.* Size-controlled stabilization of the superionic phase to room temperature in polymer-coated AgI nanoparticles. *Nature Mater.* **8**, 476–480 (2009).
15. Ohta, H. *et al.* Giant thermoelectric Seebeck coefficient of a two-dimensional electron gas in SrTiO$_3$. *Nature Mater.* **6**, 129–134 (2007).
16. Soldano, C., Mahmood, A. & Dujardin, E. Production, properties and potential of graphene. *Carbon* **48**, 2127–2150 (2010).
17. Lotya, M. *et al.* Liquid Phase Production of Graphene by Exfoliation of Graphite in Surfactant/Water Solutions. *J. Am. Chem. Soc.* **131**, 3611–3620 (2009).
18. Parades, J. I., Villar-Rodil, S., Martínez-Alonso, A. & Tascón, J. M. D. Graphene Oxide Dispersions in Organic Solvents. *Langmuir* **24**, 10560–10564 (2008).
19. Hernandez, Y. *et al.* High-yield production of graphene by liquid-phase exfoliation of graphite. *Nature Nanotech.* **3**, 563–568 (2008).
20. Cai, J. *et al.* Atomically precise bottom-up fabrication of graphene nanoribbons. *Nature* **466**, 470–473 (2010).
21. Kitagawa, S., Kitaura, R. & Noro, S. Functional Porous Coordination Polymers. *Angew. Chem., Int. Ed.* **43**, 2334–2375 (2004).
22. Férey, G. Hybrid porous solids: past, present, future. *Chem. Soc. Rev.* **37**, 191–214 (2008).
23. Zhou, H. C., Long, J. R. & Yaghi, O. M. Introduction to Metal-Organic Frameworks. *Chem. Rev.* **112**, 673–674 (2012).
24. Cook, T. R., Zheng, Y. R. & Stang, P. J. Metal-organic frameworks and self-assembled supramolecular coordination complexes: Comparing and contrasting the design, synthesis, and functionality of metal-organic materials. *Chem. Rev.* **113**, 734–777 (2013).
25. Janiak, C. Engineering coordination polymers towards applications. *Dalton Trans.* 2781–2804 (2003).
26. Li, J. R., Kuppler, R. J. & Zhou, H. C. Selective gas adsorption and separation in metal-organic frameworks. *Chem. Soc. Rev.* **38**, 1477–1504 (2009).
27. Seo, J. S. *et al.* A homochiral metal-organic porous material for enantioselective separation and catalysis. *Nature* **404**, 982–986 (2000).
28. Horcajada, P. *et al.* Porous metal-organic-framework nanoscale carriers as a potential platform for drug delivery and imaging. *Nature Mater.* **9**, 172–178 (2010).
29. Yerushalmi, R., Scherz, A. & van der Boom, M. E. Enhancement of Molecular Properties in Thin Films by Controlled Orientation of Molecular Building Blocks. *J. Am. Chem. Soc.* **126**, 2700–2701 (2004).
30. Hermes, S., Schröder, F., Chelmowski, R., Wöll, C. & Fischer, R. A. Selective Nucleation and Growth of Metal-Organic Open Framework Thin Films on Patterned COOH/CF$_3$-Terminated Self-Assembled Monolayers on Au(111). *J. Am. Chem. Soc.* **127**, 13744–13745 (2005).
31. Biemmi, E., Scherb, C. & Bein, T. Oriented Growth of the Metal Organic Framework Cu$_3$(BTC)$_2$(H$_2$O)$_3$·xH$_2$O Tunable with Functionalized Self-Assembled Monolayers. *J. Am. Chem. Soc.* **129**, 8054–8055 (2007).
32. Haruki, R. *et al.* Structural evaluation of an iron oxalate complex layer grown on an ultra-smooth sapphire (0001) surface by a wet method. *Trans. MRS-J* **33**, 629–631 (2008).
33. Zacher, D., Schmid, R., Wöll, C. & Fischer, R. A. Surface Chemistry of Metal-Organic Frameworks at the Liquid-Solid Interface. *Angew. Chem. Int. Ed.* **50**, 176–199 (2010).
34. Liu, B., Zacher, D. & Fischer, R. A. Multi Variant Surface Mounted Metal-Organic Frameworks. *Adv. Funct. Mater.* DOI: 10.1002/adfm.201202996 (2013).
35. Sakata, Y. *et al.* Shape-Memory Nanopores Induced in Coordination Frameworks by Crystal Downsizing. *Science* **339**, 193–196 (2013).
36. Makiura, R. *et al.* Surface nano-architecture of a metal–organic framework. *Nature Mater.* **9**, 565–571 (2010).
37. Makiura, R. & Kitagawa, H. Porous Porphyrin Nanoarchitectures on Surfaces. *Eur. J. Inorg. Chem.* **24**, 3715–3724 (2010).
38. Motoyama, S., Makiura, R., Sakata, O. & Kitagawa, H. Highly Crystalline Nanofilm by Layering of Porphyrin Metal-Organic Framework Sheets. *J. Am. Chem. Soc.* **133**, 5640–5643 (2011).
39. Xu, G., Yamada, T., Otsubo, K., Sakaida, S. & Kitagawa, H. Facile "Modular Assembly" for Fast Construction of a Highly Oriented Crystalline MOF Nanofilm. *J. Am. Chem. Soc.* **134**, 16524–16527 (2012).
40. Lee, H. J., Cho, Y. J., Cho, W. & Oh, M. Controlled Isotropic or Anisotropic Nanoscale Growth of Coordination Polymers: Formation of Hybrid Coordination Polymer Particles. *ACS Nano* **7**, 491–499 (2013).
41. Falcaro, P., Buso, D., Hill, A. J. & Doherty, C. M. Patterning Techniques for Metal Organic Frameworks. *Adv. Mater.* **24**, 3153–3168 (2012).
42. Roberts, G. (Ed.) Langmuir-Blodgett Films, Plenum Press, New York, 1990.
43. Smolenyak, P. *et al.* Highly Ordered Thin Films of Octasubstituted Phthalocyanines. *J. Am. Chem. Soc.* **121**, 8628–8636 (1999).
44. Cook, M. J. Langmuir-Blodgett films of phthalocyanines. *Int. J. Electronics* **76**, 727–739 (1994).
45. Qian, D.-J., Nakamura, C. & Miyake, J. Multiporphyrin Array from Interfacial Metal-Mediated Assembly and Its Langmuir-Blodgett Films. *Langmuir* **16**, 9615–9619 (2000).
46. Zhang, C.-F., Chen, M., Nakamura, C., Miyake, J. & Qian, D.-J. Electrochemically Driven Generation of Manganese(IV,V)-oxo Multiporphyrin Arrays and Their Redox Properties with Manganese(III) Species in Langmuir-Blodgett Films. *Langmuir* **24**, 13490–13495 (2008).
47. Liu, B. *et al.* Metal-mediated coordination polymer nanotubes of 5,10,15,20-tetrapyridylporphine and tris(4-pyridyl)-1,3,5-triazine at the water–chloroform interface. *Chem. Commun.* 3175–3177 (2006).
48. Li, X. *et al.* Highly conducting graphene sheets and Langmuir-Blodgett films. *Nature Nanotech.* **3**, 538–542 (2008).